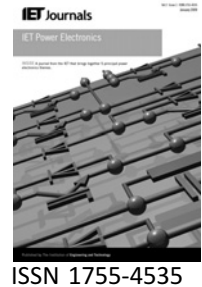


Published in IET Power Electronics  
 Received on 5th June 2009  
 Revised on 23rd August 2009  
 doi: 10.1049/iet-pel.2009.0020



# Improved switching frequency variation control of hysteresis controlled voltage source inverter-fed IM drives using current error space vector

R. Ramchand K. Sivakumar A. Das C. Patel K. Gopakumar

CEDT, Indian Institute of Science, Bangalore 560012, India  
 E-mail: kgopa@cedt.iisc.ernet.in

**Abstract:** A constant switching frequency current error space vector-based hysteresis controller for two-level voltage source inverter-fed induction motor (IM) drives is proposed in this study. The proposed controller is capable of driving the IM in the entire speed range extending to the six-step mode. The proposed controller uses the parabolic boundary, reported earlier, for vector selection in a sector, but uses simple, fast and self-adaptive sector identification logic for sector change detection in the entire modulation range. This new scheme detects the sector change using the change in direction of current error along the axes  $jA$ ,  $jB$  and  $jC$ . Most of the previous schemes use an outer boundary for sector change detection. So the current error goes outside the boundary six times during sector change, in one cycle, introducing additional fifth and seventh harmonic components in phase current. This may cause sixth harmonic torque pulsations in the motor and spread in the harmonic spectrum of phase voltage. The proposed new scheme detects the sector change fast and accurately eliminating the chance of introducing additional fifth and seventh harmonic components in phase current and provides harmonic spectrum of phase voltage, which exactly matches with that of constant switching frequency voltage-controlled space vector pulse width modulation (VC-SVPWM)-based two-level inverter-fed drives.

## 1 Introduction

Voltage source inverters (VSI) used for generating sinusoidal fundamental voltage with variable frequency and voltage can be either voltage controlled or current controlled [1–20]. Current-controlled pulse width modulated (PWM) VSIs are preferred for high performance ac drives [21]. Among the different current-controlled PWM techniques, hysteresis-band current-controlled PWM method is popularly used because of its inherent simplicity and fast dynamic response [1–20]. But the major drawbacks associated with conventional hysteresis controller-based PWM techniques are limit-cycle oscillations, non-optimum current ripple and random switching of voltage vectors [1, 2]. Current error space vector (CESV)-based fixed tolerance band hysteresis controller-based PWM methods

eliminate these problems associated with conventional hysteresis controllers [4–9, 13]. But the major problem associated with the conventional as well as the CESV-based hysteresis controllers is large variation in the switching frequency over the entire operating speed range of the motor [1–9, 13]. This causes excess harmonic current and switching losses leading to additional machine heating. In [10] optimum PWM performance is obtained by using an adaptive hysteresis-band controller, which is programmed as a function of load and supply parameters. Sinusoidal band hysteresis controller proposed in [11] requires extra lockout circuit for keeping the average switching frequency equivalent to that of a fixed band hysteresis controller causing distortion in current. Hysteresis current controller (HCC) for the PWM rectifier proposed in [14, 15] does not prevent the variation in

switching frequency for the entire operating speed range of the motor. Modular hysteresis controller for multi-level inverters is proposed in [17]. It does not discuss about the switching frequency variations. In [18], a continuously varying parabolic boundary for the CESV is proposed to get the switching frequency variation pattern of the output voltage of the HC-based PWM inverter similar to that of voltage-controlled space vector pulse width modulation (VC-SVPWM)-based VSI. But the major problem associated with this technique is the requirement of extra outer parabola for the identification of sector change which gives rise to some switching frequency variations in one fundamental cycle and over the entire operating speed range. It also introduces fifth and seventh harmonic components in the voltage causing fifth and seventh harmonic currents in the induction motor. These harmonic currents may cause sixth harmonic torque pulsations in the machine, especially in low speed operation.

This paper proposes a new technique for sector change detection replacing the outer parabola proposed in [18]. The proposed method uses current errors along  $jA$ ,  $jB$  and  $jC$  axes, which are orthogonal to  $A$ ,  $B$  and  $C$  axes, respectively, for detecting the sector change, so that a fast and accurate detection of sector change is possible. This makes the voltage harmonic spectrum of the proposed hysteresis controller-based inverter exactly matching with that of a constant switching frequency space vector PWM (SVPWM)-based inverter. This technique uses the property that the current error along one of the orthogonal axis changes its direction during sector change [5, 8]. So the current error never goes outside the parabolic boundary, when compared to outer parabola-based sector change technique in [18]. So the proposed new technique for sector change eliminates the fifth and seventh harmonic components from the inverter output voltage and suppresses the sixth harmonic torque pulsations in the motor. Using this scheme for sector change and parabolic boundary for CESV, simulation study is carried out for steady state performance of the proposed and VC-SVPWM-based controllers. Simulation results are experimentally verified for the entire operating speed range of the motor up to six-step mode of operation, for the present proposed modified controller.

## 2 CESV variation in VC-SVPWM-based IM drive

Figs. 1a and b, respectively, show the power circuit of a two-level VSI-fed IM drive and the voltage space vector structure generated by that inverter. This VSI-fed IM drive can be controlled by voltage-control or current-control principle [8, 13]. In the VC-SVPWM-based inverter fed IM drives the switching frequency of the inverter remains constant since the PWM switching interval ( $T_s$ ) is kept constant [8, 13]. For a given switching frequency, for the position of reference voltage space vector in any triangular sector (any one of 1, 2, ..., 6 of Fig. 1b), the switching times for active

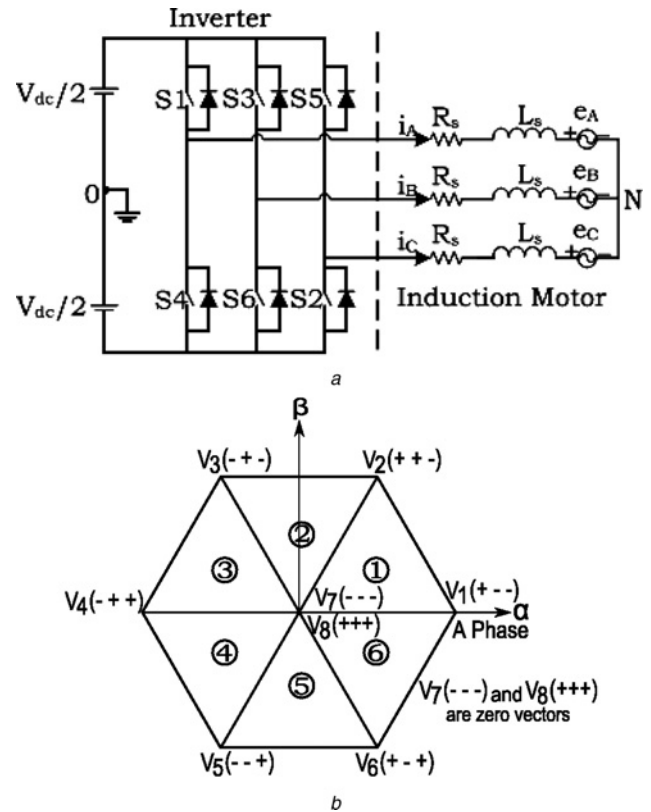


**Figure 1** Schematic of the two-level inverter structure  
 a Power schematic of a three-phase two-level VSI-fed IM drive  
 b Voltage space vector structure of a three-phase two-level VSI-fed IM drive

voltage vectors (any two of  $V_1, V_2, \dots, V_6$  of Fig. 1b for particular sector) and zero voltage vectors ( $V_7$  and  $V_8$  of Fig. 1b) are decided based on the voltage-time (volt-second) balance principle. CESV for the inverter of Fig. 1a is given by  $\Delta i = i - i^*$  ( $i$  is the current space vector and  $i^*$  is the reference current space vector). For machine voltage vector  $V_m$  in sector 1, the expressions for CESV when vectors  $V_1, V_2$  and  $V_0$  are switched on can be represented as [5, 8]

$$\Delta i_{(V_1)} = \frac{\Delta V_{(V_1)}}{L_\sigma} t, \Delta i_{(V_2)} = \frac{\Delta V_{(V_2)}}{L_\sigma} t \text{ and } \Delta i_{(V_0)} = \frac{\Delta V_{(V_0)}}{L_\sigma} t \quad (1)$$

where  $L_\sigma$  is the stator leakage inductance.

The trajectories of  $\Delta i$  obtained for different positions of  $V_m$  (in a sector), for 10–40 Hz operation, are plotted on the  $\alpha - \beta$  plane and its extreme points are joined using interpolation to get a continuous curve for all the six sectors. This gives the theoretical boundary for CESV for  $V_m$  in all the sectors. Fig. 2a shows the boundary obtained for the different sectors during 10 Hz operation. The approximated boundaries of CESV for position of  $V_m$  in sector 2, for various operating speeds of the motor, for constant switching frequency VC-SVPWM-based two-level VSI-fed IM drive are found as shown in Fig. 2b.

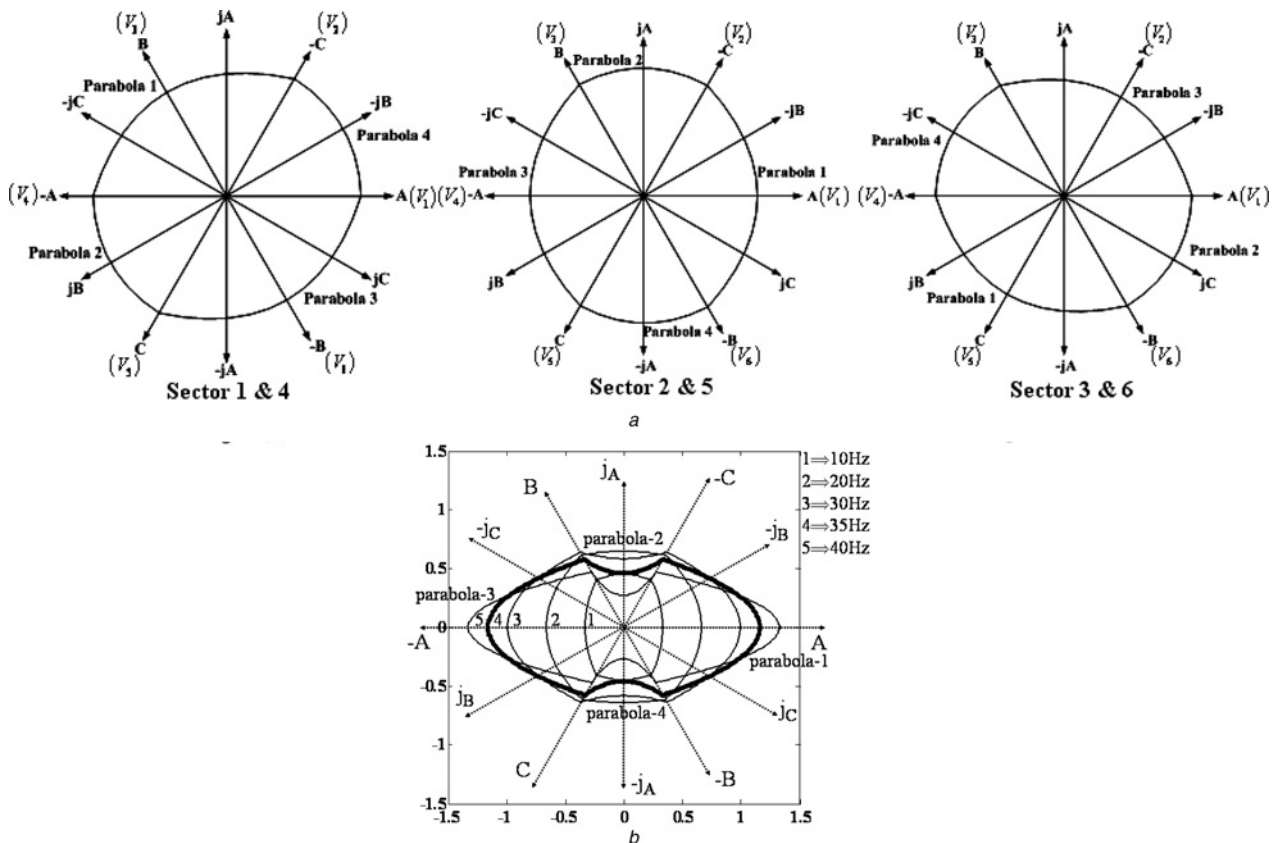


**Figure 2** Current error space phasor boundary for space vector PWM

a Theoretical boundary obtained by interpolation for CESV for 10 Hz operation

b Approximated boundary of CESV for position of  $V_m$  in sector 2 for various operating speeds of the motor for the constant switching frequency VC-SVPWM-based two-level VSI-fed IM drive

Similarly, the boundaries of  $\Delta i$  for position of  $V_m$  in all the six sectors of Fig. 1b can be formulated for different speeds of machine in linear range of operation.

The boundary of  $\Delta i$  in sector 2 shown in Fig. 2 can be approximated as a set of four unique parabolas (parabola 1 between axes  $-C$  and  $-B$ , parabola 2 between  $-C$  and  $B$ , parabola 3 between  $C$  and  $B$ , parabola 4 between  $-B$  and  $C$ ). But the vertex and the focus of these four parabolas keep on changing with respect to the speed of the machine. If the axis of a parabola is vertical (conventional  $Y$  axis), and the vertex is at  $(h, k)$ , then the parabola can be uniquely characterised by (2), where  $p$  is the distance between vertex and focus of the parabola. In a similar way, a horizontal parabola (parabola axis is conventional  $X$  axis) with vertex  $(h, k)$  is given by (3). Using (1)–(3), a generalised algorithm is developed.

$$(x - h)^2 = 4p(y - k) \tag{2}$$

$$(y - k)^2 = 4p(x - h) \tag{3}$$

It takes only four parameters as input (dc-link voltage  $V_{dc}$  of inverter, base speed of the machine, stator leakage inductance ( $L_\sigma$ ) of the machine and switching frequency  $f_s$ ) and provides

the unique sets of vertex, focus and intersecting points of four parabolas for any given speed of the motor. This algorithm is implemented using Matlab program and its output is fed to the Simulink model file for online variation of the boundary of  $\Delta i$  (in 1 Hz step) from 1 to 45 Hz (end of the linear range of operation) operation of any given machine. For over-modulation mode of operation (above 45 Hz) the boundary of  $\Delta i$  is maintained the same as that is used for 45 Hz operation. In this work the amplitude of CESV is monitored along  $A, B, C, jA, jB$  and  $jC$  axes for vector selection and sector change detection. The  $X$  and  $Y$  axes of parabolas used for vector selection will be decided by the sector in which the machine voltage space vector lies. Table 1 gives the  $X$  and  $Y$  axes for parabolas in different sectors. The vector selection using parabolic boundary is implemented using simple look up table whose detailed

**Table 1** Equivalent  $X$  and  $Y$  axes for the parabolas of current error space phasor boundary in different sectors

Sectors	$X$ axis	$Y$ axis
1, 4	$B$	$jB$
2, 5	$A$	$jA$
3, 6	$C$	$jC$

explanation is available in [18]. In this paper a new sector change detection scheme is proposed. The proposed scheme is explained in the following section.

### 3 Sector change detection in proposed controller

Whenever the machine voltage vector ( $V_m^*$ ) moves from one sector to the next sector, the current error will first decrease and then increase along a unique axis, which is the axis perpendicular to the boundary of the sectors involved. As an example, for forward rotation of machine (anticlockwise movement of the  $V_m^*$ ) sector change from sector 1 to sector 2 is detected along the  $jC$  axis by providing an extra outer parabolic boundary (Fig. 3a).

In this paper we are proposing a new scheme for sector change detection for the hysteresis current controlled two-level inverter. Fig. 3a shows that when the machine back EMF vector is moving from sector 1 to sector 2 the current error along the  $jC$  axis changes its direction before increasing and hitting the outer boundary. Fig. 3a clearly shows that when vector 2, vector 7 or vector 8 is switched on, the current error along the  $jC$  axis has the same direction, when machine back emf vector is in sector 1. But, when the machine back emf vector reaches sector 2, the current error along the  $jC$  axis changes its direction for the same vectors. Similarly, other sector changes are associated with a change in direction of current error along any one of the orthogonal axes ( $jA$ ,  $jB$  or  $jC$ ). Fig. 3b shows the current error along the  $jA$  axis for a VC-SVPWM-based inverter. A close examination of Fig. 3b shows that, for SVPWM-based inverter the current error along the  $jA$  axis changes its direction (at point C of Fig. 3b) during the sector change. This point is detected in the present scheme for enabling the sector change, so that an improved switching frequency variation control of current hysteresis-controlled PWM scheme can be realised. When sector changes from 6 to 1 or 3 to 4 (Fig. 1b), there is a direction change in current error along the  $jA$  axis. Similarly, when sector changes from 1 to 2 or 4 to 5

**Table 2** Proposed sector change detection logic for forward rotation of machine

Present sector	Present vector "ON"	Axis along which there will be change in direction of current error during sector change					
		1	2	3	4	5	6
1	$V_2$ or $V_7$ or $V_8$	*	$jC$	*	*	*	*
2	$V_3$ or $V_7$ or $V_8$	*	*	$jB$	*	*	*
3	$V_4$ or $V_7$ or $V_8$	*	*	*	$jA$	*	*
4	$V_5$ or $V_7$ or $V_8$	*	*	*	*	$jC$	*
5	$V_6$ or $V_7$ or $V_8$	*	*	*	*	*	$jB$
6	$V_1$ or $V_7$ or $V_8$	$jA$	*	*	*	*	*

\*Continue with the same sector

(Fig. 1b) there is a direction change in current error along the  $jC$  axis and for a sector change from 2 to 3 or 5 to 6 (Fig. 1b) there is a direction change in current error along the  $jB$  axis. Table 2 shows the proposed new sector change logic for forward rotation of the motor. In the proposed new scheme this direction change along orthogonal axes is detected as explained below.

Consider that the machine voltage vector is moving from sector 1 to sector 2 as shown in Fig. 3a. The vectors that will be switched in sector 1 are 1, 2, 7 and 8 (1 and 2 are active vectors and 7 and 8 are zero vectors) (Fig. 1b). Whenever vector 2, 7 or 8 is switched on, the value of the current error along the  $jC$  axis is stored in a memory location. Now, after a time period ( $\Delta t$ ) the difference between the present value and the stored value of the current error along the  $jC$  axis is calculated. This difference obtained is stored in another memory location. This difference is calculated after every  $\Delta t$  period. If there is no sector change this difference value increases linearly.

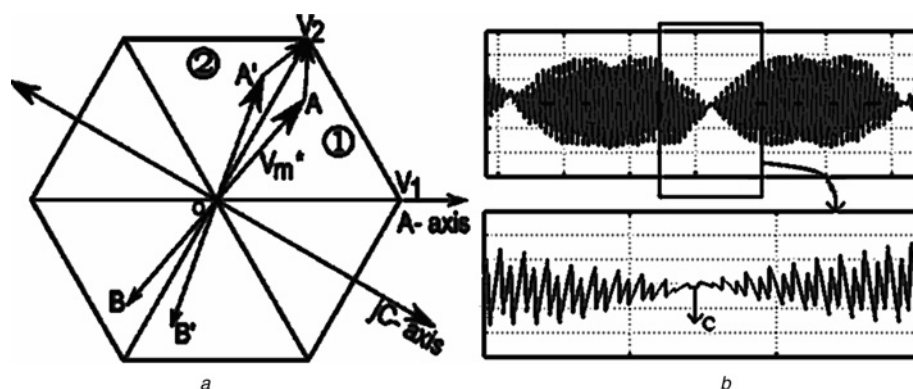


**Figure 3** Reference vector transition from sector-2 to sector-3 and current error change

a Current error during sector 1 to sector 2 change  
b Current error along the  $jA$  axis during sector change

But, during sector change this difference value starts decreasing. By comparing the present and previous values of this difference, we will decide whether a change of

sector has occurred or not. The value of  $\Delta t$  is chosen as a fraction of the fundamental period. The criterion for selecting  $\Delta t$  is that it should be much less than one-sixth

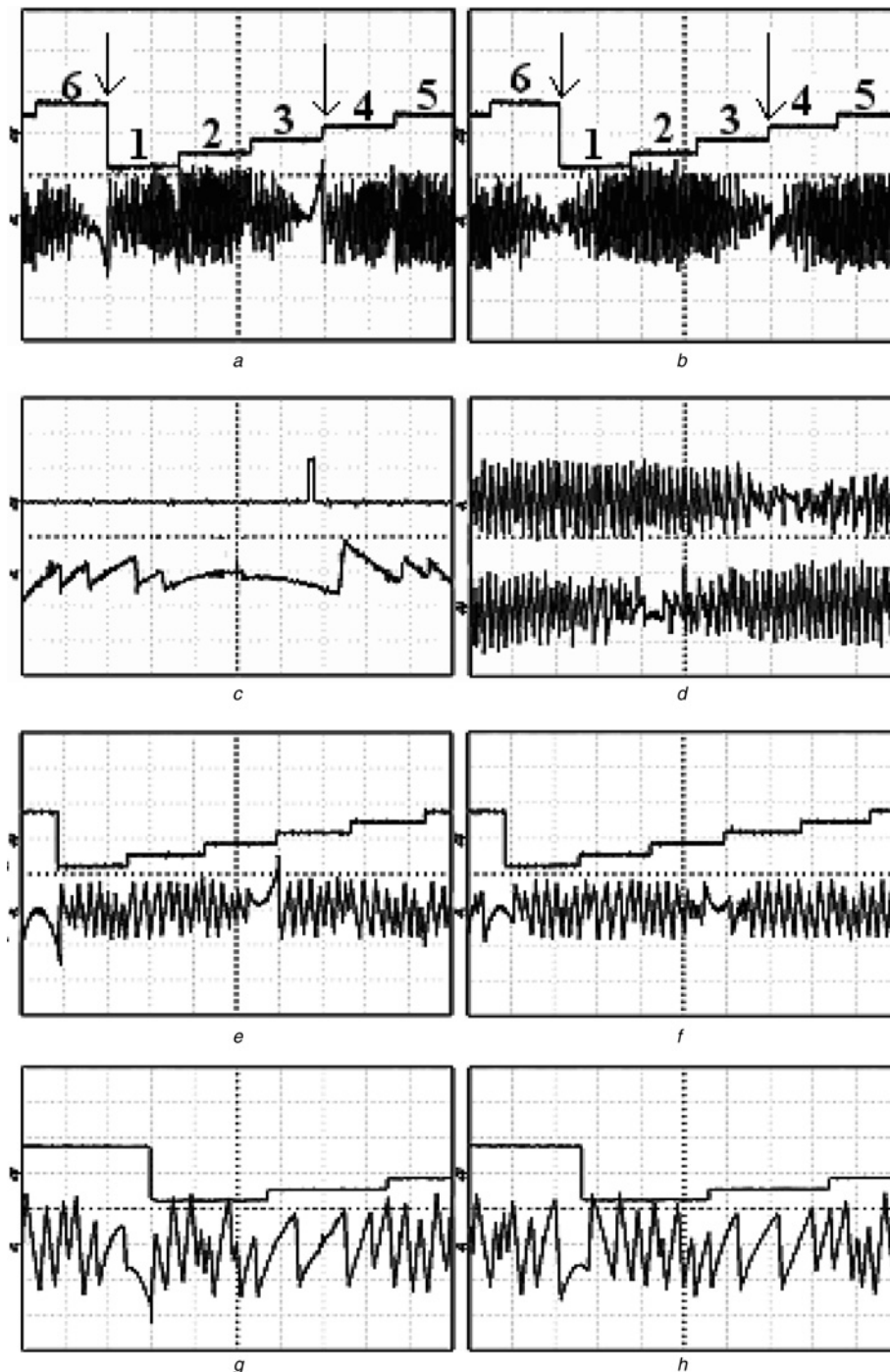


**Figure 4** Experimental results

- a* Sector and current error along the  $jA$  axis at 10 Hz for the controller with outer parabola  
*b* Sector and current error along the  $jA$  axis at 10 Hz for the proposed controller (X axis: 10 ms/div. and Y axis: 2/div., 0.25 A/div.)  
*c* Output of sector detection circuit and current error along the  $jA$  axis at 10 Hz for the proposed controller (X axis: 1 ms/div. and Y axis: 2/div., 0.25 A/div.)  
*d* Current error along  $jA$  and  $jB$  axes for the proposed controller at 10 Hz (X axis: 5 ms/div. and Y axis: 0.5 A/div.)  
*e* Sector and current error along the  $jA$  axis at 20 Hz for the controller with outer parabola  
*f* Sector and current error along the  $jA$  axis at 20 Hz for the proposed controller (X axis: 5 ms/div. and Y axis: 2/div., 0.25 A/div.)  
*g* Sector and current error along the  $jA$  axis at 40 Hz for the controller with outer parabola  
*h* Sector and current error along the  $jA$  axis at 40 Hz for the proposed controller (X axis: 1.5 ms/div. and Y axis: 2/div., 0.25 A/div.)

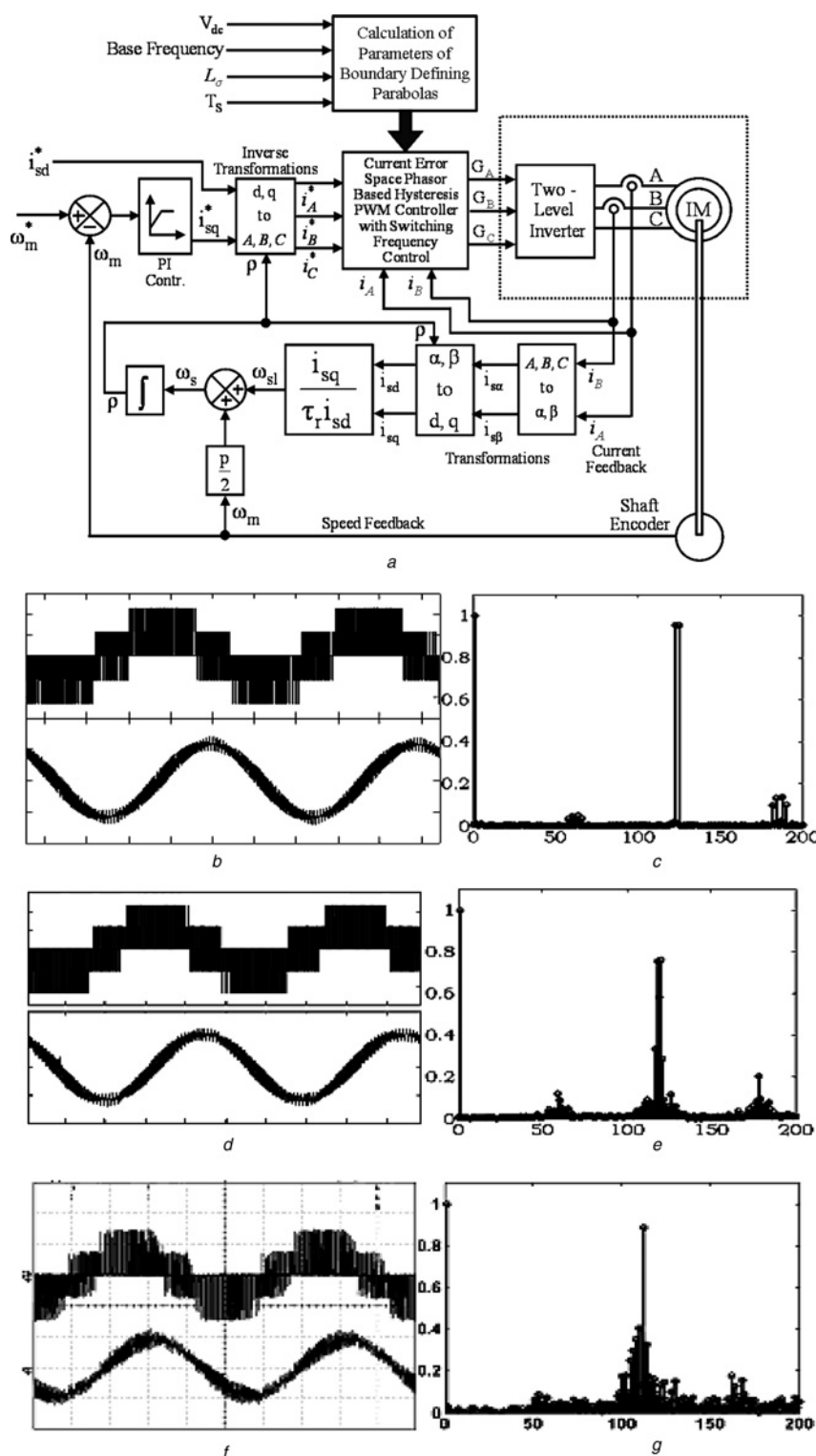


**Figure 5** Simulation results

*a* Block schematic of the proposed hysteresis PWM controller for two-level VSI-fed IM drive

*b* Phase voltage, phase current for VC-SVPWM at 10 Hz (simulation results) (X axis: 20 ms/div. and Y axis: 100 V/div., 1 A/div.)

*c* Normalised harmonic spectrum of phase voltage for VC-SVPWM at 10 Hz (simulation results) (X axis: 50/div. and Y axis: 0.2/div.)

*d* Phase voltage, phase current for the proposed hysteresis controller at 10 Hz (simulation results) (X axis: 20 ms/div. and Y axis: 100 V/div., 1 A/div.)

*e* Normalised harmonic spectrum of phase voltage for the proposed hysteresis controller at 10 Hz (simulation results) (X axis: 50/div. and Y axis: 0.2/div.)

*f* Phase voltage, phase current for the proposed hysteresis controller at 10 Hz (experimental results) (X axis: 20 ms/div. and Y axis: 100 V/div., 1 A/div.)

*g* Normalised harmonic spectrum of phase voltage for the proposed hysteresis controller at 10 Hz (experimental results) (X axis: 50/div. and Y axis: 0.2/div.)

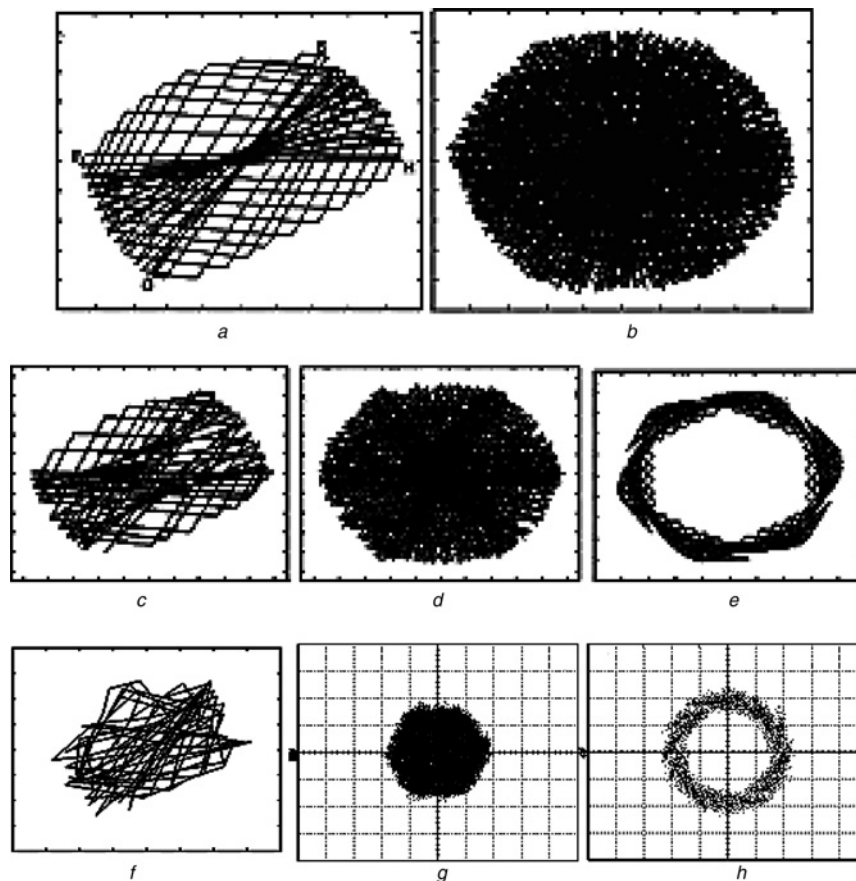


**Figure 6** Current error space vector – simulation study

- a* CESV for sector 1 for VC-SVPWM at 10 Hz (simulation results)  
*b* CESV for one cycle for VC-SVPWM at 10 Hz (simulation results) (X axis: 0.1 A/div. and Y axis: 0.1 A/div.)  
*c* CESV for sector 1 for the proposed hysteresis controller at 10 Hz (simulation results) (X axis: 0.1 A/div. and Y axis: 0.1 A/div.)  
*d* CESV for one cycle for the proposed hysteresis controller at 10 Hz (simulation results) (X axis: 0.1 A/div. and Y axis: 0.1 A/div.)  
*e* Current space phasor for one cycle for the proposed hysteresis controller at 10 Hz (simulation results) (X axis: 0.5 A/div. and Y axis: 0.5 A/div.)  
*f* CESV for sector 1 the proposed hysteresis controller at 10 Hz (experimental results) (X axis: 0.1 A/div. and Y axis: 0.1 A/div.)  
*g* CESV for one cycle the proposed hysteresis controller at 10 Hz (experimental results) (X axis: 0.1 A/div. and Y axis: 0.1 A/div.)  
*h* Current space phasor for one cycle for the proposed hysteresis controller at 10 Hz (experimental results) (X axis: 0.5 A/div. and Y axis: 0.5 A/div.)

of the fundamental period. For the implementation of the proposed new scheme the value of  $\Delta t$  used is 1.5% of the fundamental period, which is one order less than one-sixth.

The performance of the proposed sector change detection scheme is compared with outer parabola-based sector change detection scheme proposed in [18]. Fig. 4a shows the experimental results for the hysteresis controller using outer parabola for sector change detection at 10 Hz. In Fig. 4a, top trace shows sector variation and bottom trace shows current error along the  $jA$  axis for one cycle of operation at 10 Hz. It clearly shows that during sector 6 to 1 and sector 3 to 4 changes the current error along the  $jA$  axis goes outside the boundary. Similarly, during other sector changes the current error goes outside the boundary along the  $jB$  and  $jC$  axes. There are six sector changes in a cycle, so

current error goes outside the boundary six times in one cycle. This introduces additional fifth and seventh harmonic components in phase current. In Fig. 4b, top trace is sector variation and bottom trace is current error along the  $jA$  axis for the proposed hysteresis controller for one cycle of operation at 10 Hz. Fig. 4b clearly shows that current error is not going outside the parabolic boundary during sector change. So the proposed scheme will not introduce additional fifth and seventh harmonic components in phase current as the controller proposed in [18]. In Fig. 4c top trace shows output of sector change detection block and bottom trace shows current error along the  $jA$  axis for the proposed controller at 10 Hz. Accurate and fast sector change detection, using the proposed controller, can be clearly seen from Fig. 4c. Fig. 4d shows current error along  $jA$  and  $jB$  axes for the proposed controller at 10 Hz. Figs. 4e and g show the sector variation and

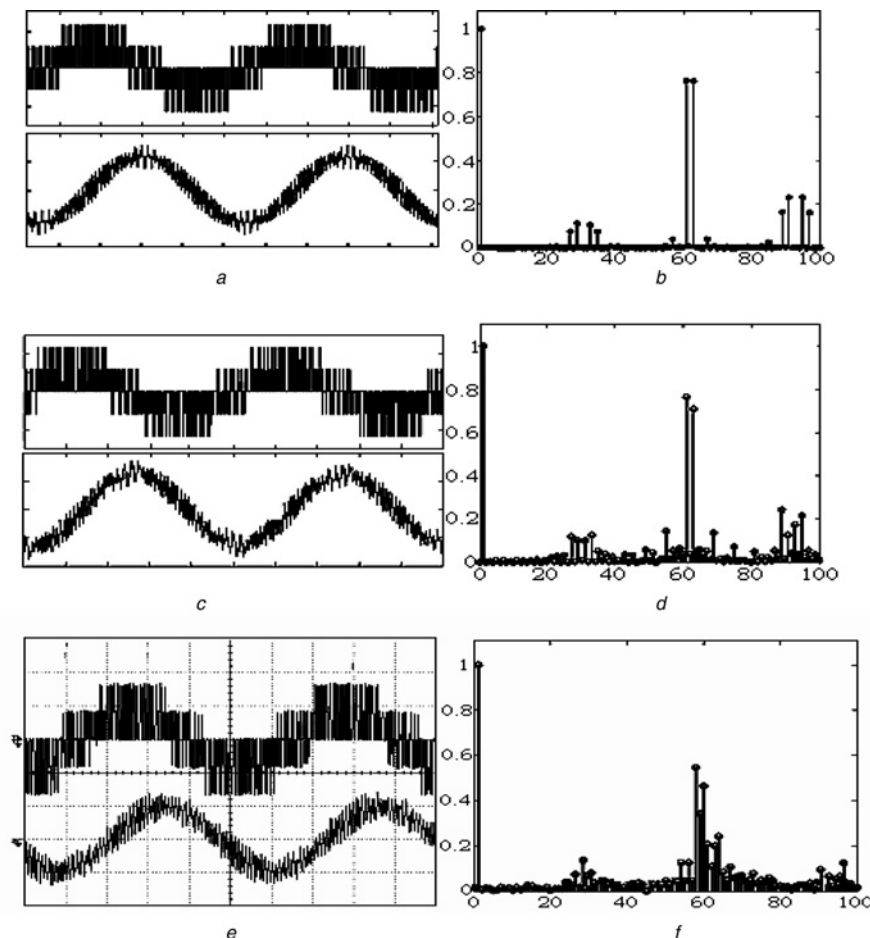


**Figure 7** Phase voltage and phase current – simulation study-20 Hz

*a* Phase voltage, phase current for VC-SVPWM at 20 Hz (simulation results) (X axis: 10 ms/div. and Y axis: 100 V/div., 1 A/div.)

*b* Normalised harmonic spectrum of phase voltage for VC-SVPWM at 20 Hz (simulation results) (X axis: 20/div. and Y axis: 0.2/div.)

*c* Phase voltage, phase current for the proposed hysteresis controller at 20 Hz (simulation results) (X axis: 10 ms/div. and Y axis: 100 V/div., 1 A/div.)

*d* Normalised harmonic spectrum of phase voltage for the proposed hysteresis controller at 20 Hz (simulation results) (X axis: 20/div. and Y axis: 0.2/div.)

*e* Phase voltage, phase current for the proposed hysteresis controller at 20 Hz (experimental results) (X axis: 10 ms/div. and Y axis: 100 V/div., 1 A/div.)

*f* Normalised harmonic spectrum of phase voltage for the proposed hysteresis controller at 20 Hz (experimental results) (X axis: 20/div. and Y axis: 0.2/div.)

current error along the  $jA$  axis for hysteresis controller with outer parabola, at 20 and 40 Hz. Figs. 4*f* and *b* show the sector variation and current error along the  $jA$  axis for the proposed hysteresis controller with new sector change detection scheme, at 20 and 40 Hz.

## 4 Simulation and experimental results of the proposed hysteresis controller

A detailed simulation study of the constant switching frequency VC-SVPWM-based inverter and the proposed hysteresis controller scheme are carried out using Simulink toolbox on Matlab platform. The performance of the proposed controller is then experimentally verified on a 3.7 kW IM drive fed with a two-level VSI using

vector control. The block schematic of the proposed hysteresis PWM controller is shown in Fig. 5*a*. The parameters of the 3.7 kW IM used in the simulation studies are given in the Appendix. Figs. 5*b* and *c* and Figs. 6*a* and *b* show the simulation results for constant switching frequency VC-SVPWM-based inverter at 10 Hz. In Fig. 5*b* top trace is phase voltage and bottom trace is phase current. Fig. 5*c* shows normalised harmonic spectrum of phase voltage. Fig. 6*a* shows the CESV trajectory when machine back emf vector is in sector 1 and Fig. 6*b* shows the CESV trajectory for one cycle of operation. Figs. 5*d* and *e* and Figs. 6*c*–*e* show the simulation results for the proposed hysteresis controller at 10 Hz. In Fig. 5*d* top trace is phase voltage and bottom trace is phase current. Fig. 5*e* shows normalised harmonic spectrum of phase voltage. Fig. 6*c* shows the CESV trajectory when machine fundamental voltage vector is in

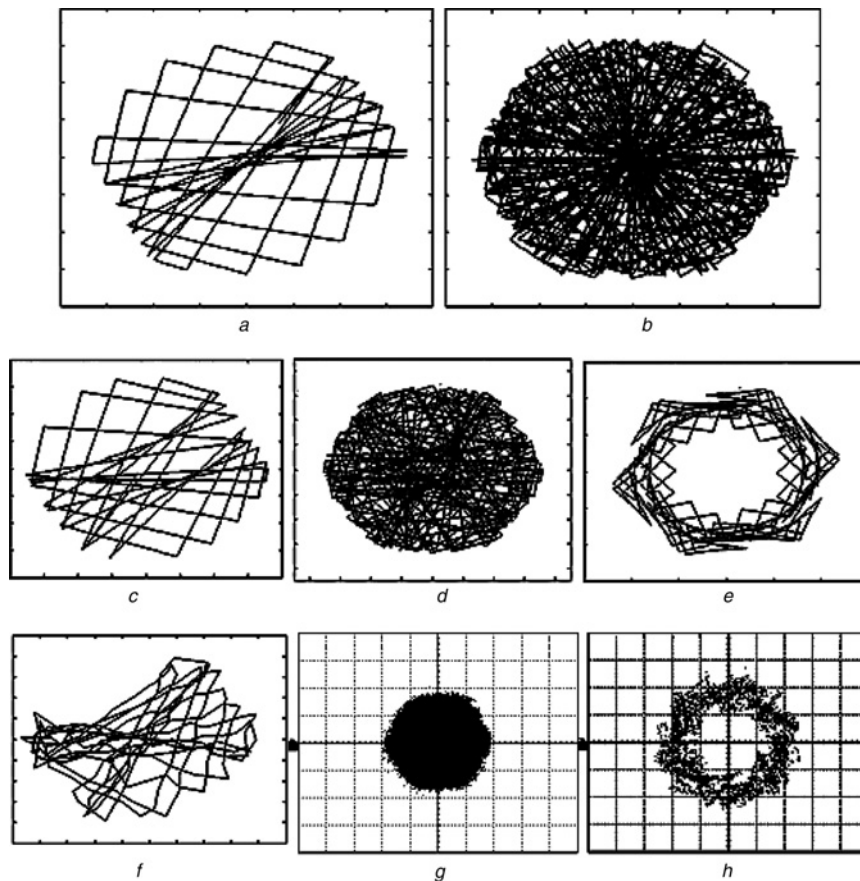


**Figure 8** Current error space vectors – simulation study-20 Hz

- a* CESV for sector 1 for VC-SVPWM at 20 Hz (simulation results) (X axis: 0.2 A/div. and Y axis: 0.2 A/div.)  
*b* CESV for one cycle for VC-SVPWM at 20 Hz (simulation results) (X axis: 0.2 A/div. and Y axis: 0.2 A/div.)  
*c* CESV for sector 1 for the proposed hysteresis controller at 20 Hz (simulation results) (X axis: 0.2 A/div. and Y axis: 0.2 A/div.)  
*d* CESV for one cycle for the proposed hysteresis controller at 20 Hz (simulation results) (X axis: 0.2 A/div. and Y axis: 0.2 A/div.)  
*e* Current space vector for one cycle for the proposed hysteresis controller at 20 Hz (simulation results) (X axis: 1 A/div. and Y axis: 1 A/div.)  
*f* CESV for sector 1 for the proposed hysteresis controller at 20 Hz (experimental results) (X axis: 0.2 A/div. and Y axis: 0.2 A/div.)  
*g* CESV for one cycle for the proposed hysteresis controller at 20 Hz (experimental results) (X axis: 0.2 A/div. and Y axis: 0.2 A/div.)  
*h* Current space phasor for one cycle for the proposed hysteresis controller at 20 Hz (experimental results) (X axis: 1 A/div. and Y axis: 1 A/div.)

sector 1, Fig. 6*d* shows the CESV trajectory for one cycle of operation and Fig. 6*e* current space vector for one cycle of operation. Figs. 5*f* and 5*g* and Figs. 6*f*–*h* show the experimental results for the proposed hysteresis controller at 10 Hz. In Fig. 5*f* top trace is phase voltage and bottom trace is phase current. Fig. 5*g* shows normalised harmonic spectrum of phase voltage. Fig. 6*f* shows the CESV trajectory when machine back emf vector is in sector 1, Fig. 6*g* shows the CESV trajectory for one cycle of operation and Fig. 6*h* current space vector for one cycle of operation. If we compare the fast Fourier transform (FFT) of phase voltage obtained for the proposed controller with FFT of the phase voltage for controller with outer parabolas proposed in [18], we can see that the fifth and seventh harmonic components are highly suppressed and the spread in the spectrum is also reduced. So the phase voltage harmonic spectrum of the proposed controller is exactly matching with that of the

VC-SVPWM-based inverter giving a constant switching frequency of 1.25 kHz.

Simulation results in Fig. 7*a* shows phase voltage and phase current for VC-SVPWM at 20 Hz. Fig. 7*b* shows normalised harmonic spectrum of phase voltage shown in Fig. 7*a*. Simulation results in Fig. 7*c* show phase voltage and phase current for the proposed controller at 20 Hz. Fig. 7*d* shows normalised harmonic spectrum of phase voltage shown in Fig. 7*c*. Experimental results in Fig. 7*e* show phase voltage and phase current for the proposed controller at 20 Hz. Fig. 7*f* shows the normalised harmonic spectrum of phase voltage shown in Fig. 7*e*. The results show that phase voltage harmonic spectrum of CESV shows in sector 1 and CESV in one cycle for VC-SVPWM at 20 Hz. Simulation results of Figs. 8*a* and *b* show CESV in sector 1 and CESV in one cycle for VC-SVPWM at 20 Hz. Simulation results of Fig. 8*c*–*e* show CESV in sector 1, CESV in one cycle and

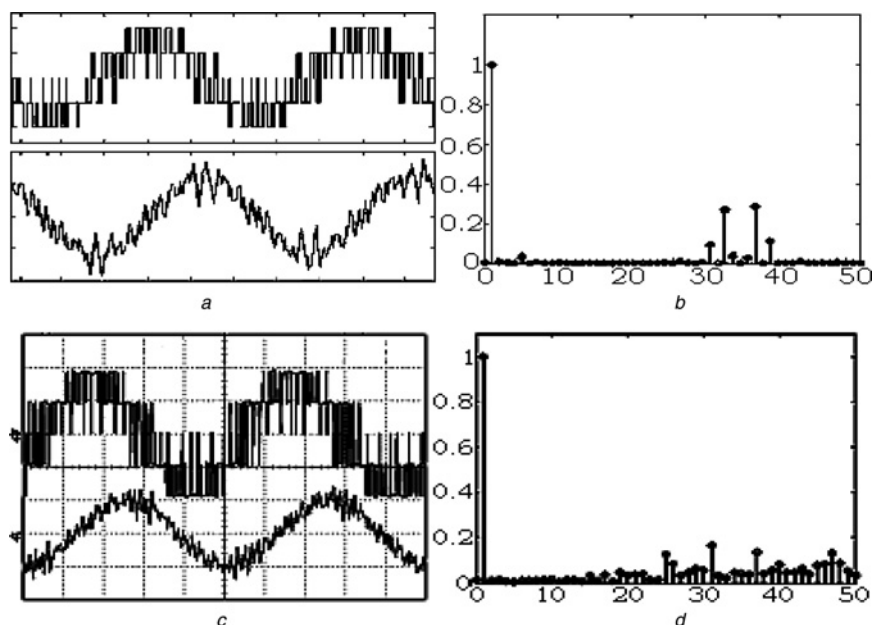


**Figure 9** Phase voltage and phase current – simulation study-40 Hz

*a* Phase voltage, phase current for VC-SVPWM at 40 Hz (simulation results) (X axis: 5 ms/div. and Y axis: 100 V/div., 1 A/div.)

*b* Normalised harmonic spectrum of phase voltage for VC-SVPWM at 40 Hz (simulation results) (X axis: 10/div. and Y axis: 0.2/div.)

*c* Phase voltage, phase current for the proposed hysteresis controller at 40 Hz (experimental results) (X axis: 5 ms/div. and Y-axis: 100 V/div, 1 A/div.)

*d* Normalised harmonic spectrum of phase voltage for the proposed hysteresis controller at 40 Hz (experimental results) (X axis: 10/div. and Y axis: 0.2/div.)

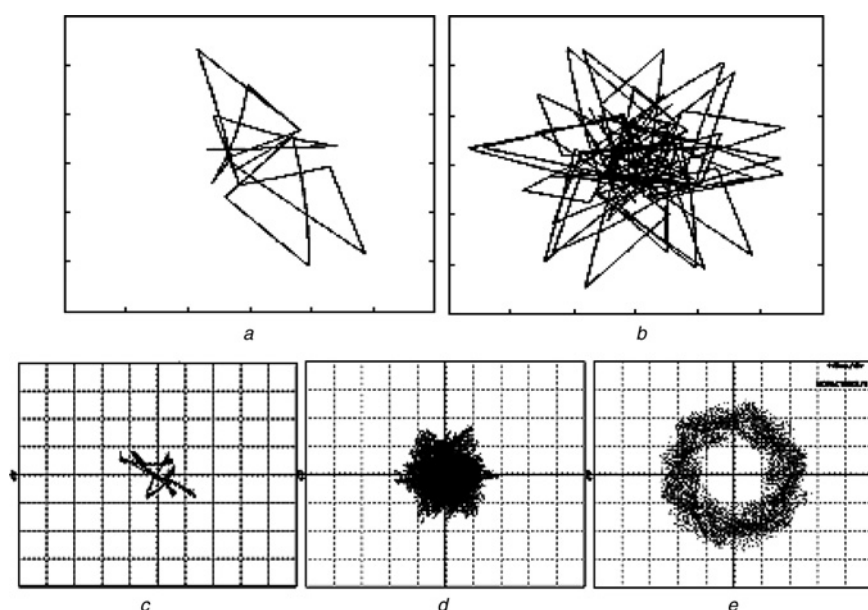


**Figure 10** Current error space vectors – simulation study-40 Hz

*a* CESV for sector 1 for VC-SVPWM at 40 Hz (simulation results) (X axis: 0.5 A/div. and Y axis: 0.5 A/div.)

*b* CESV for one cycle for VC-SVPWM at 40 Hz (simulation results) (X axis: 0.5 A/div. and Y axis: 0.5 A/div.)

*c* CESV for sector 1 for the proposed hysteresis controller at 40 Hz (experimental results) (X axis: 0.5 A/div. and Y axis: 0.5 A/div.)

*d* CESV for one cycle for the proposed hysteresis controller at 40 Hz (experimental results) (X axis: 0.5 A/div. and Y axis: 0.5 A/div.)

*e* Current space phasor for one cycle for the proposed hysteresis controller at 40 Hz (experimental results) (X axis: 1 A/div. and Y axis: 1 A/div.)

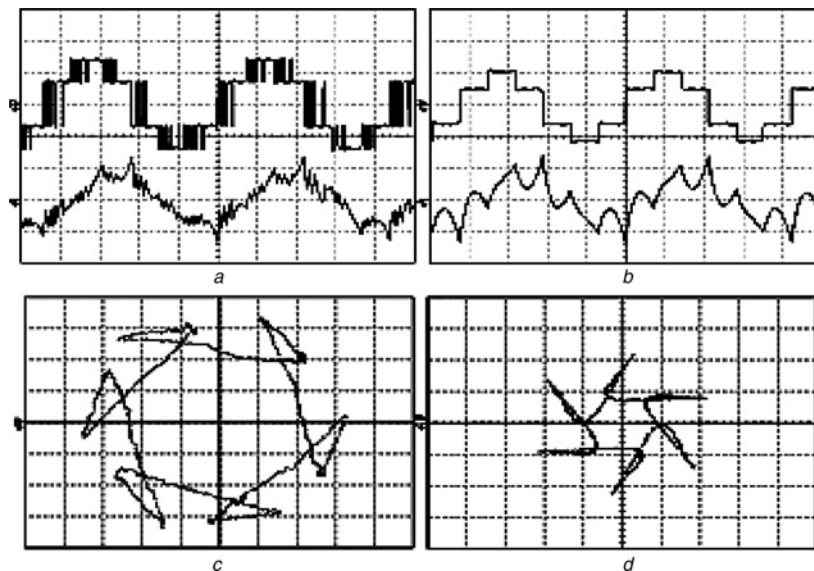
current space vector in one cycle for the proposed controller at 20 Hz. Experimental results of Figs. 8*f–h* show CESV in sector 1, CESV in one cycle and current space vector in one

cycle for the proposed controller at 20 Hz. Fig. 9 shows the results for 40 Hz operation. Figs. 9*a* and *b* show phase voltage, phase current and normalised harmonic spectrum of

phase voltage for VC-SVPWM at 40 Hz (Simulation Results). Figs. 9c and d show phase voltage, phase current and normalised harmonic spectrum of phase voltage for the proposed hysteresis controller at 40 Hz (Experimental Results). Figs. 10a and b show the simulation results of CESV in one sector and CESV in one cycle for VC-SVPWM at 40 Hz. Figs. 10c–e show the experimental results of CESV in one sector, CESV in one cycle and current space vector in one cycle for the proposed controller at 40 Hz. From experimental and

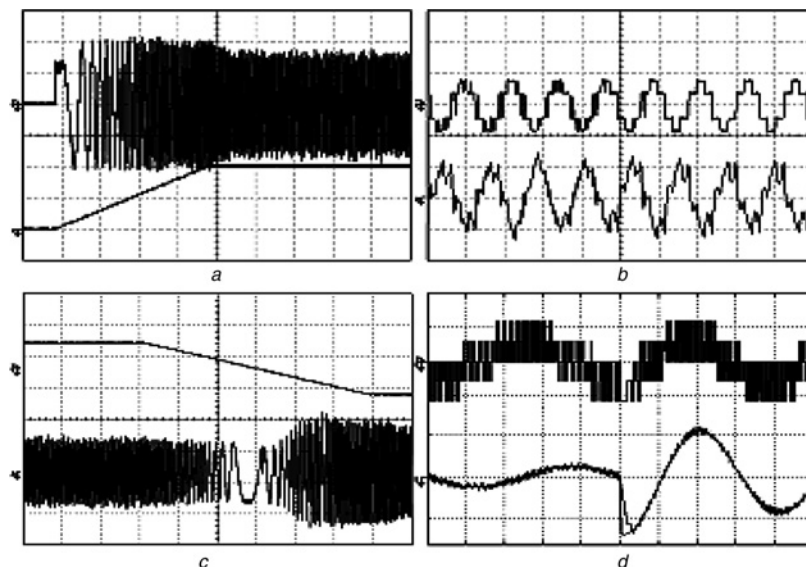
simulation results, we can see that the harmonic spectrum of phase voltage is improved, with the elimination of fifth and seventh harmonic components, in the proposed controller for the entire linear modulation range.

Fig. 11 shows the experimental results for the proposed hysteresis controller during over modulation and six-step mode operation. Phase voltage and phase current at 47 Hz (over modulation) are shown in Fig. 11a. From



**Figure 11** Experimental results for the proposed hysteresis controller

- a Phase voltage and phase current at 47 Hz operation (over modulation) (X axis: 5 ms/div. and Y axis: 100 V/div., 1 A/div.)  
 b Phase voltage and phase current at 50 Hz operation (six-step mode) (X axis: 5 ms/div. and Y axis: 100 V/div., 1 A/div.)  
 c Current error space phasor for one cycle for six-step mode operation (X axis: 0.2 A/div. and Y axis: 0.2 A/div.)  
 d Current space phasor for one cycle for six-step mode operation (X axis: 1 A/div. and Y axis: 1 A/div.)



**Figure 12** Experimental results for the proposed hysteresis controller

- a Phase current and speed during acceleration from stand still to 20 Hz (X axis: 1 s/div. and Y axis: 1 A/div., 10 Hz/div.)  
 b Phase voltage and phase current during transition from over modulation to six-step mode (X axis: 1 s/div. and Y axis: 100 V/div., 1 A/div.)  
 c Speed reversal from 10 to -20 Hz (X axis: 1 s/div. and Y axis: 10 Hz/div., 1 A/div.)  
 d Phase voltage and phase current when a 2 A step change is applied in  $I_{sq}^*$  (X axis: 10 ms/div. and Y axis: 100 V/div., 1 A/div.)

Fig. 11*b*, we can see phase voltage and phase current during six-step mode operation (50 Hz). CESV boundary for one cycle at 47 Hz and six-step operation are shown in Figs. 11*c* and *d*.

Fig. 12 shows the experimental results for the transient performance of the proposed hysteresis controller. Fig. 12*a* shows phase current and speed during acceleration of the motor from stand still to 20 Hz. Fig. 12*b* shows the transition from over modulation to six-step mode during acceleration of the motor from 40 to 50 Hz. Fig. 12*c* shows the speed reversal transient for the motor using the proposed hysteresis controller. It shows the speed reversal from 10 to -20 Hz. Fig. 12*d* shows the phase voltage and phase current overlapped with reference current when a step change in  $I_{sq}^*$  ( $q$ -axis stator reference current) is applied. When a step change of 2 A is applied to  $I_{sq}^*$ , how the controller is able to track that change is demonstrated in Fig. 12*d*.

## 5 Conclusion

In this paper, a CESV-based simple hysteresis PWM controller is proposed to eliminate the switching frequency variation in the two-level PWM inverter-fed IM drives. A parabolic boundary for the CESV is used in this paper for getting the switching frequency pattern in the output voltage of hysteresis controller similar to that of the constant switching frequency VC-SVPWM-based VSI-fed IM drive. In this paper a new scheme for sector change detection without using outer boundaries is proposed. Exact resemblance of switching frequency spectrum obtained using proposed scheme and VC-SVPWM-based drive is proved with the help of extensive simulation and experimental studies. Sector change logic is self-adaptive and is capable of taking the drive up to six-step mode, if needed. The steady state and transient performance of the proposed controller is experimentally verified on a 3.7 kW IM drive in the entire operating range up to the six-step mode of operation. It is shown that the experimental results are in the good agreement with the simulation results for the proposed drive. All other inherent advantages of space vector-based HCC, such as, adjacent voltage vector switching, no machine back emf calculation and fast dynamic response are retained in the proposed scheme in addition to elimination of switching frequency variation.

## 6 References

- [1] RAHMAN M.A., RADWAN T.S., OSHEIBA A.M., LASHINE A.E.: 'Analysis of current controllers for voltage-source inverter', *IEEE Trans. Ind. Electron.*, 1997, **44**, (4), pp. 477–485
- [2] KAZMIERKOWSKI M.P., MALESANI L.: 'Current control techniques for three-phase voltage-source PWM converters: a survey', *IEEE Trans. Ind. Electron.*, 1998, **45**, (5), pp. 691–703
- [3] NAGY I.: 'Novel adaptive tolerance band based PWM for field-oriented control of induction machines', *IEEE Trans. Ind. Electron.*, 1994, **41**, (4), pp. 406–417
- [4] NAGY I.: 'Improved current controller for PWM inverter drives with the background of chaotic dynamics'. IECON'94, 5–9 September 1994, pp. 561–566
- [5] MISTRY V., WAIKER S.P., GOPAKUMAR K., UMANAND L., RANGANATHAN V.T.: 'A multi axis space phasor based current hysteresis controller for PWM inverters', *EPE J.*, 2000, **10**, (1), pp. 17–25
- [6] KAZMIERKOWSKI M.P., DZIENIAKOWSKI M.A., SULKOWSKI W.: 'Novel space vector based current controllers for PWM-inverters', *IEEE Trans. Power Electron.*, 1991, **6**, (1), pp. 158–166
- [7] PAN C.T., CHANG T.Y.: 'An improved hysteresis current controller for reducing switching frequency', *IEEE Trans. Power Electron.*, 1994, **9**, (1), pp. 97–104
- [8] BAIJU M.R., MOHAPATRA K.K., KANCHAN R.S., TEKWANI P.N., GOPAKUMAR K.: 'A space phasor based current hysteresis controller using adjacent inverter voltage vectors with smooth transition to six step operation for a three phase voltage source inverter', *EPE J.*, 2005, **15**, (1), pp. 36–47
- [9] TEKWANI P.N., KANCHAN R.S., GOPAKUMAR K.: 'Current-error spacevector-based hysteresis PWM controller for three-level voltage source inverter fed drives', *IEE Proc. EPA*, 2005, **152**, (5), pp. 1283–1295
- [10] BOSE B.K.: 'An adaptive hysteresis-band current control technique for a voltage-fed PWM inverter for machine drive system', *IEEE Trans. Ind. Electron.*, 1990, **37**, (5), pp. 402–408
- [11] TRIPATHI A., SEN P.C.: 'Comparative analysis of fixed and sinusoidal band hysteresis current controllers for voltage source inverters', *IEEE Trans. Ind. Electron.*, 1992, **39**, (1), pp. 63–73
- [12] MALESANI L., MATTAVELLI P., TOMASIN P.: 'Improved constant frequency hysteresis current control for VSI inverters with simple feedforward bandwidth prediction', *IEEE Trans. Ind. Appl.*, 1997, **33**, (5), pp. 1194–1202
- [13] KWON B.H., MIN B.D., YOUM J.H.: 'An improved space-vector-based hysteresis current controller', *IEEE Trans. Ind. Electron.*, 1998, **54**, (5), pp. 752–760
- [14] MIN B.-D., YOUM J.-H., KWON B.-H.: 'SVM-based hysteresis current controller for three-phase PWM rectifier', *IEE Proc.-EPA*, 1999, **146**, (2), pp. 225–230
- [15] TIWARI A.N., AGARWAL P., SRIVASTAVA S.P.: 'Modified hysteresis controlled PWM rectifier', *IEE Proc.-EPA*, 2003, **150**, (4), pp. 389–396

- [16] LIN B.-R., YANG T.-Y.: 'Experimental verification of three-phase four-wire current-regulated PWM converter', *IEE Proc.-EPA*, 2005, **152**, (3), pp. 677–685
- [17] LOH P.C., BODE G.H., TAN P.-C.: 'Modular hysteresis current control of hybrid multilevel inverters', *IEE Proc.-EPA*, 2005, **152**, (1), pp. 1–8
- [18] TEKWANI P.N., KANCHAN R.S., GOPAKUMAR K.: 'Novel current error space phasor based hysteresis controller using parabolic bands for control of switching frequency variations', *IEEE Trans. Ind. Electron.*, 2007, **54**, (5), pp. 2648–2656
- [19] NAGY I., BACKHAUSZ L.: 'Current control of VSI-PWM inverters for vector controlled drives'. Proc. 25th European Conf. Intelligent Motion, PCIM-1994, 28–30 June 1994, pp. 397–413
- [20] NAGY I., SUTO Z., BACKHAUSZ L.: 'Periodic states of hysteresis current control of induction motor'. in'. Proc. 29th European Conf. Intelligent Motion, PCIM-1996, 21–23 May 1996, pp. 605–619
- [21] FINCH J.W., GIAOURIS D.: 'Controlled AC electrical drives', *IEEE Trans. Ind. Electron.*, 2008, **55**, (2), pp. 481–491

## 7 Appendix

IM parameters: 3.7 kW, 3 $\Phi$ ; rated voltage: 415 V, 50 Hz; rated speed: 1445 rpm; 4 poles,  $R_s = 4.8 \Omega$ ,  $R_r = 3.8 \Omega$ ,  $L_s = 0.5632$  H,  $L_r = 0.577$  H and  $M = 0.546$  H.